Supplementary Material

Sub-4 nm mapping of donor-acceptor organic semiconductor nanoparticle composition

Ingemar Persson,[1,2] Hugo Laval,[3] Sylvain Chambon,[4] Gwenael Bonfante,[4] Kazuhiko Hirakawa,[4] Guillaume Wantz,[3] Benjamin Watts,[5] Matthew A. Marcus,[6] Xiaoxue Xu,[7] Lei Ying,[8] Girish Lakhwani,[9,10] Mats R. Andersson,[11] Julie M. Cairney,[1,12] Natalie P. Holmes[1,10,12]*

[1] Australian Centre for Microscopy and Microanalysis, University of Sydney, Sydney, NSW 2006, Australia.

[2] Thin Film Physics, Department of Physics, Chemistry and Biology (IFM), Linköping University, SE-58183 Linköping, Sweden.

[3] University of Bordeaux, IMS, CNRS, UMR 5218, Bordeaux INP, ENSCBP, F-33405 Talence, France.

[4] LIMMS/CNRS-IIS (IRL2820), Institute of Industrial Science, The University of Tokyo, 4-6-1 Komaba, Meguro-ku, Tokyo, 153-8505, Japan.

[5] Paul Scherrer Institute, 5232 Villigen-PSI, Switzerland.

[6] Advanced Light Source, Lawrence Berkeley National Laboratory, Berkeley, CA 94720, USA.

[7] School of Biomedical Engineering, Faculty of Engineering and Information Technology, University of Technology Sydney, NSW 2007, Australia.

[8] Institute of Polymer Optoelectronic Materials and Devices, State Key Laboratory of Luminescent Materials and Devices, South China University of Technology, Guangzhou 510640, P. R. China.

[9] ARC Centre of Excellence in Exciton Science, School of Chemistry, University of Sydney, Sydney, NSW 2006, Australia.

[10] The University of Sydney Nano Institute, Faculty of Science, University of Sydney, Sydney, NSW 2006, Australia.

[11] Flinders Institute for Nanoscale Science and Technology, Flinders University, Adelaide, South Australia 5042, Australia.

[12] School of Aerospace, Mechanical and Mechatronic Engineering, University of Sydney, Sydney, NSW 2006, Australia.

* Corresponding Author: natalie.holmes@sydney.edu.au

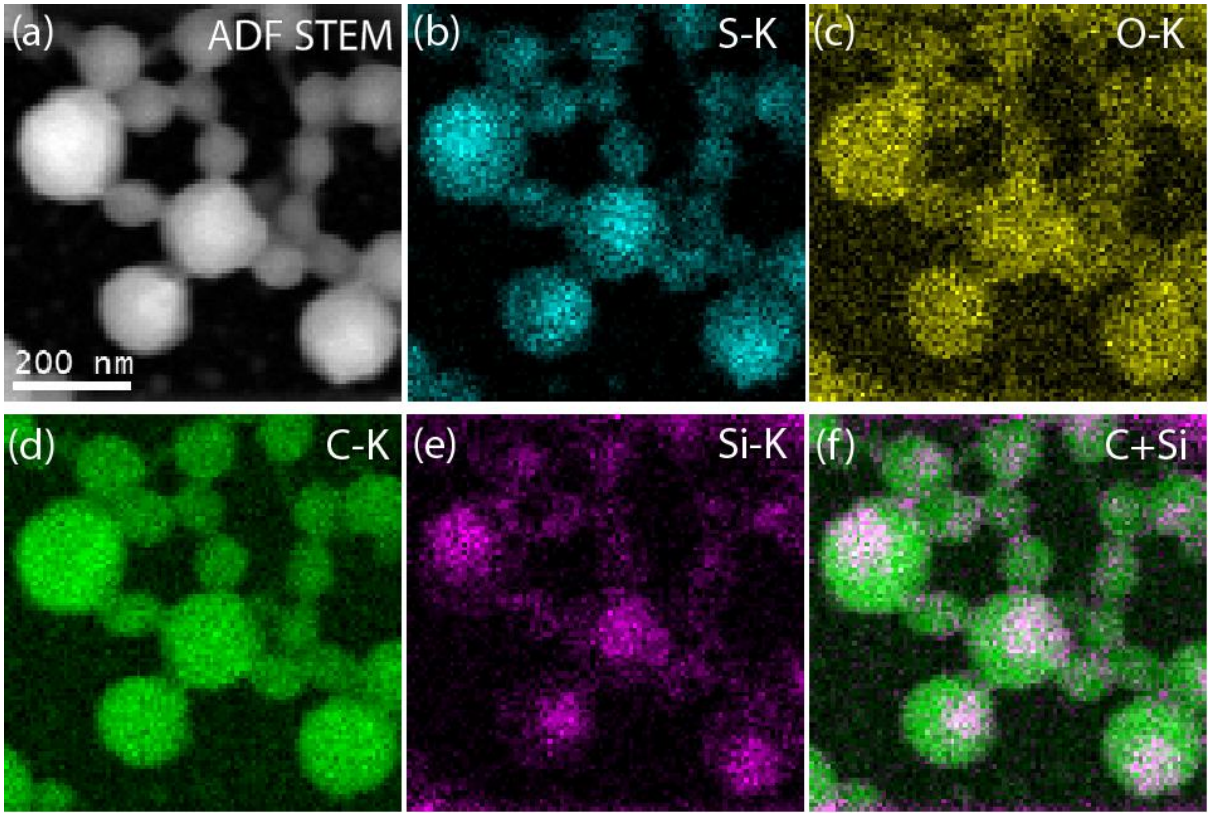

Fig. S1. Additional STEM EDX maps of PTzBI-Si:N2200 nanoparticles showing Si (purple) unique to PTzBI-Si donor polymer (and S (blue) at higher loading in the donor polymer) which occupies the core of the core-shell nanoparticles. Including overlay in (f).

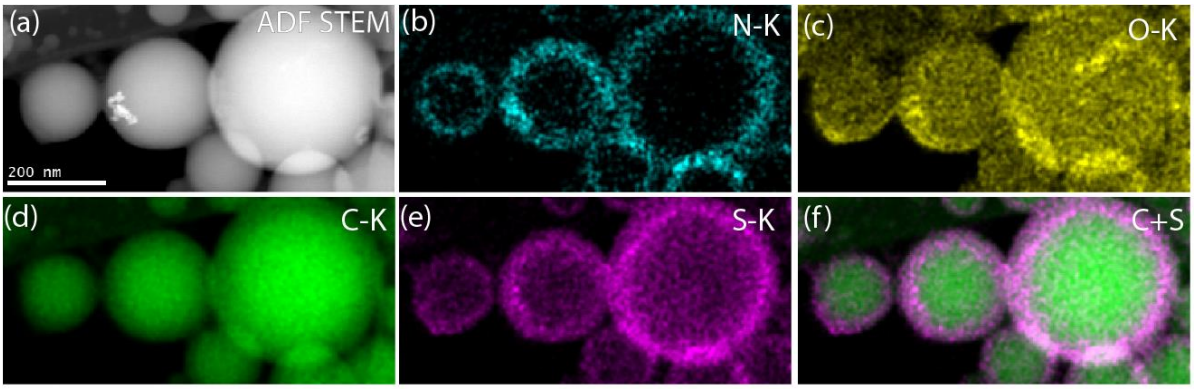

Fig. S2. Additional STEM EDX maps of TQ1:$PC_{71}BM$ nanoparticles showing N (blue) and S (purple) unique to TQ1 donor polymer which occupies the shell of the core-shell nanoparticles.. Including overlay in (f).

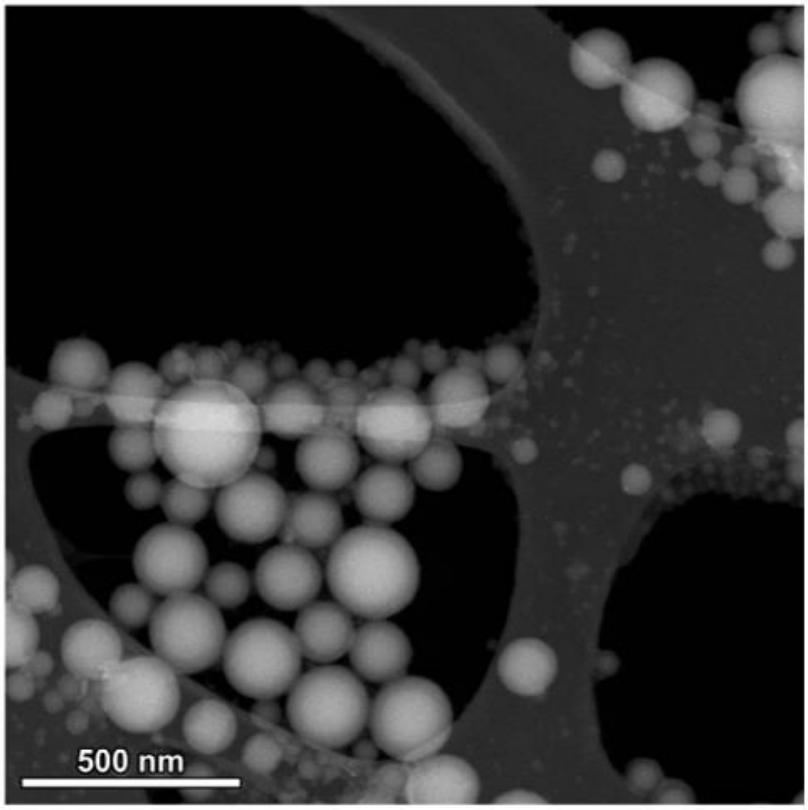

Fig. S3. High resolution STEM ADF image of TQ1:$PC_{71}BM$ nanoparticles.

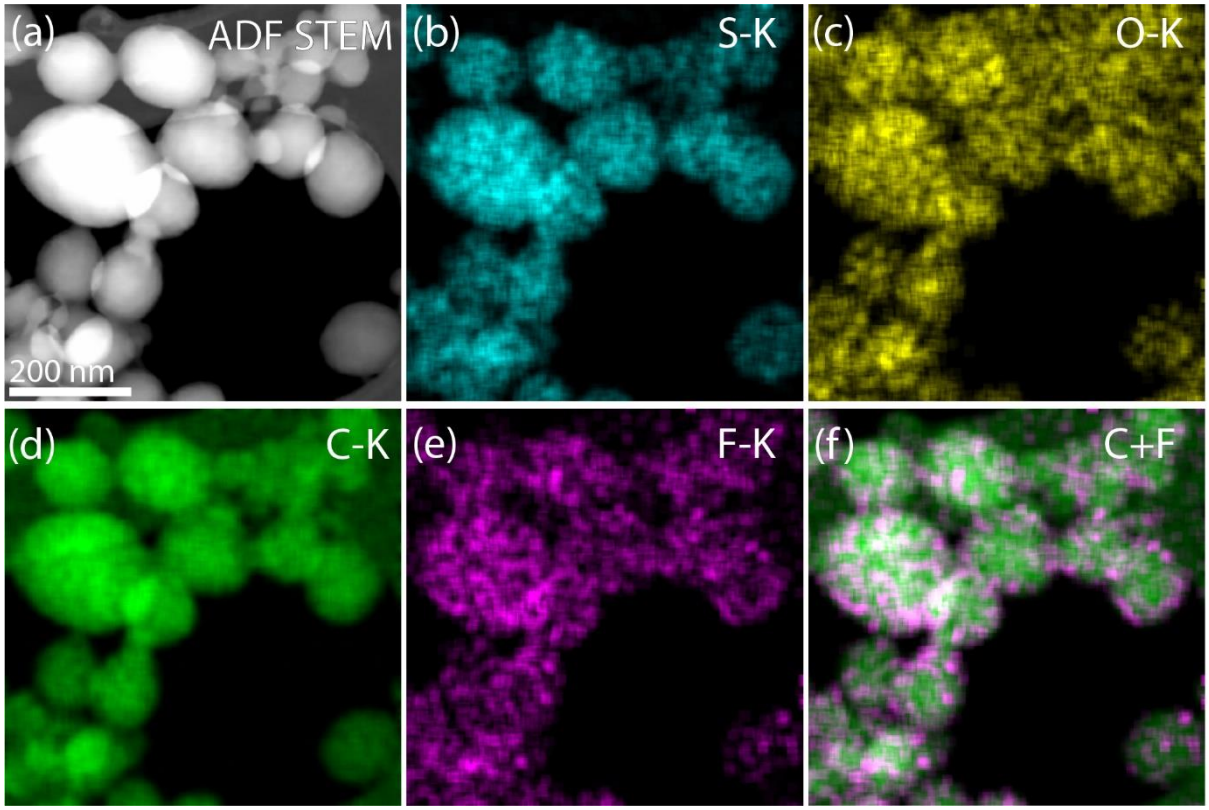

Fig. S4. Additional STEM EDX maps of 1:1 PTQ10:IDIC nanoparticles showing F (purple) unique to PTQ10 donor polymer (which occupies the shell of the core-shell nanoparticles) is not useful here for accurately mapping the shell domain.

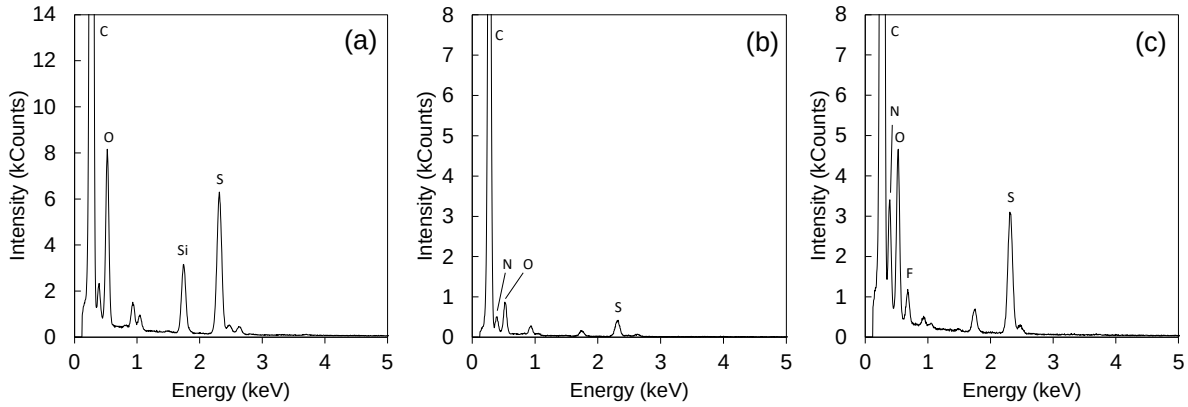

Fig. S5. EDX spectra collected in STEM-EDX mode of (a) PTzBI-Si:N2200, (b) TQ1:$PC_{71}BM$ and (c) PTQ10:IDIC nanoparticles. The peaks have been annotated with contributing elements. Background signals of Cu (0.9 keV) in (a-c) and Si (1.8 keV) in (b, c) originate from the Cu TEM grid and the EDX Si drift detector, respectively.

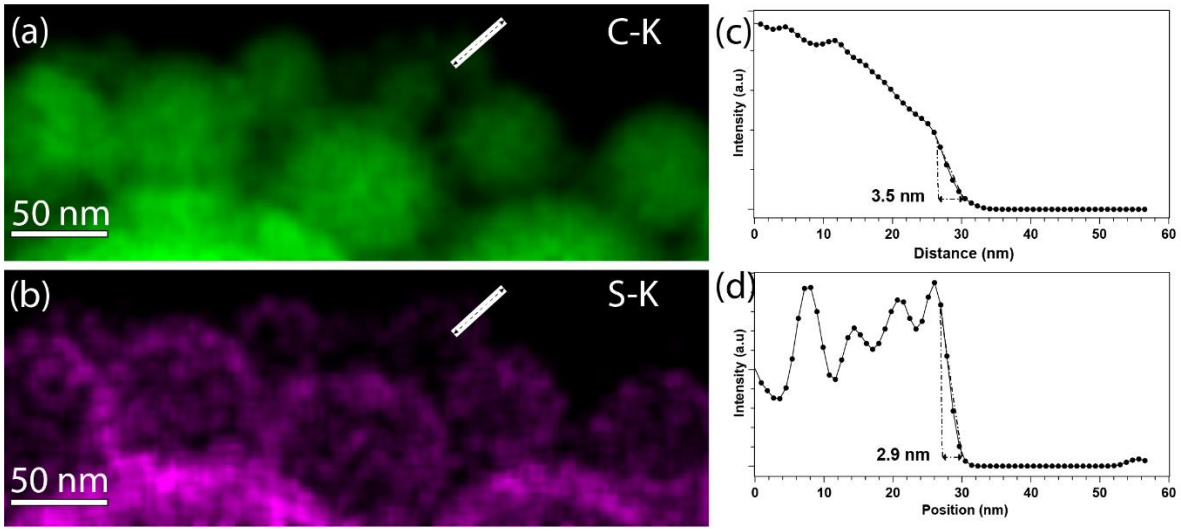

Fig. S6. Estimation of the resolution limit of STEM EDX mapping by measuring the edge spread function. (a) C-K map with a line profile indicated by a black arrow on white background across a 20 nm TQ1:$PC_{71}BM$ nanoparticle that is close to the observable limit for EDX composition gradients. (b) The corresponding STEM EDX map of S-K. (c) C-K resolution estimate via rising slope width measurement (10%-90%) of the vacuum/particle interface (3.5 nm). (d) S-K resolution estimate at 2.9 nm. The probe size for STEM is on the order of 0.1 nm and the pixel size is 0.89 nm.

The nanoparticle size distributions plotted in Figure 1e-g were generated from applying a circular Hough transform algorithm in MATLAB to SEM images of nanoparticle films (Figure 1b-d). Further particle size analysis was performed on high magnification, high resolution STEM images to account for nanoparticles of diameter <50 nm which are traditionally not captured in SEM size analysis which uses large area survey scans (magnification x20,000). These additional size distribution plots are provided here in Figure S7.

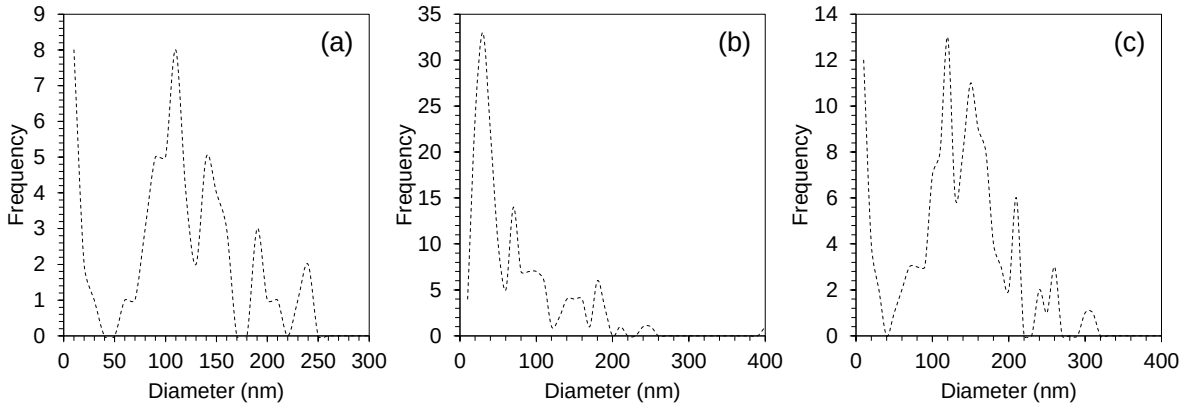

Fig. S7. Particle size distribution plots generated from high magnification, high resolution STEM images for (a) PTzBI-Si:N2200 nanoparticles (sample size n = 60), (b) TQ1:$PC_{71}BM$ nanoparticles (sample size n = 168), and (c) PTQ10:IDIC nanoparticles (sample size n = 123).

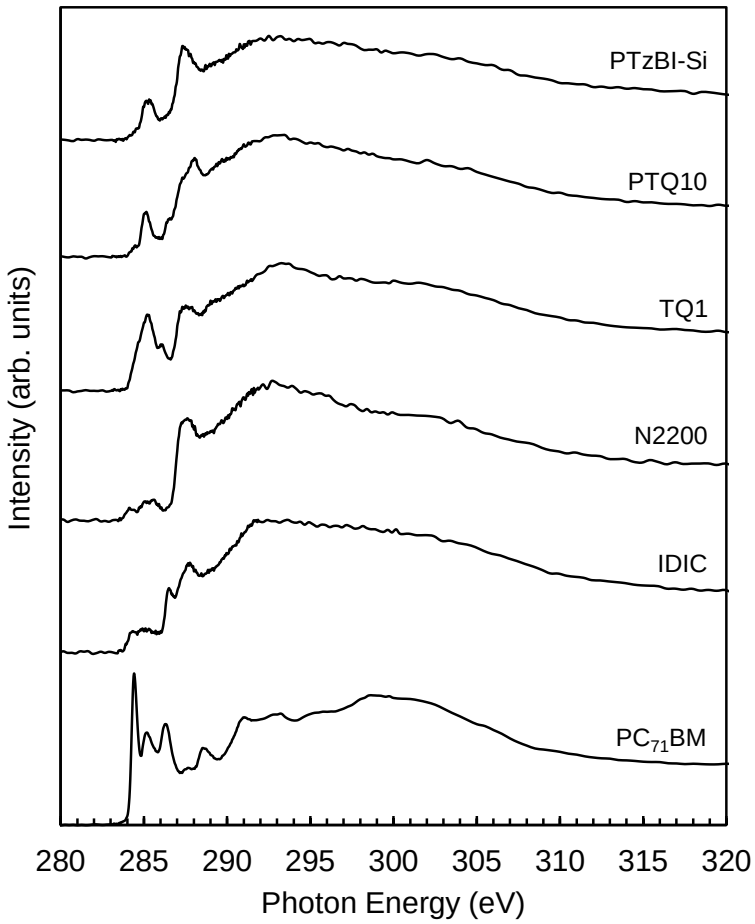

Fig. S8. NEXAFS spectra of PTzBI-Si, PTQ10, TQ1 donor polymers and N2200, IDIC and $PC_{71}BM$ non-fullerene and fullerene acceptors.

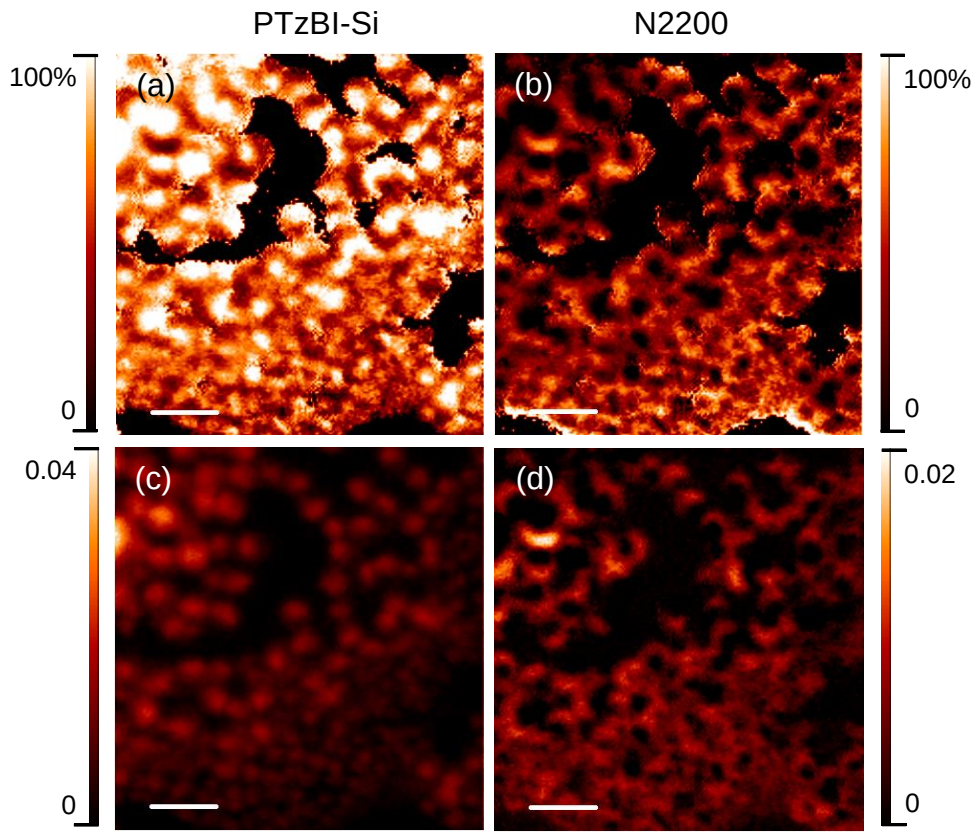

Fig . S9. STXM fractional composition maps showing the concentration of (a) PTzBI-Si and (b) N2200 with corresponding STXM mass plots (c and d) for 1:1 PTzBI-Si : N2200 nanoparticles. All scale bars are 500 nm. The colour contrast is scaled such that light colours correspond to higher component concentrations. For the mass plots (c, d) the colour scale bars indicate concentration of component in $mg.cm^{-2}$.

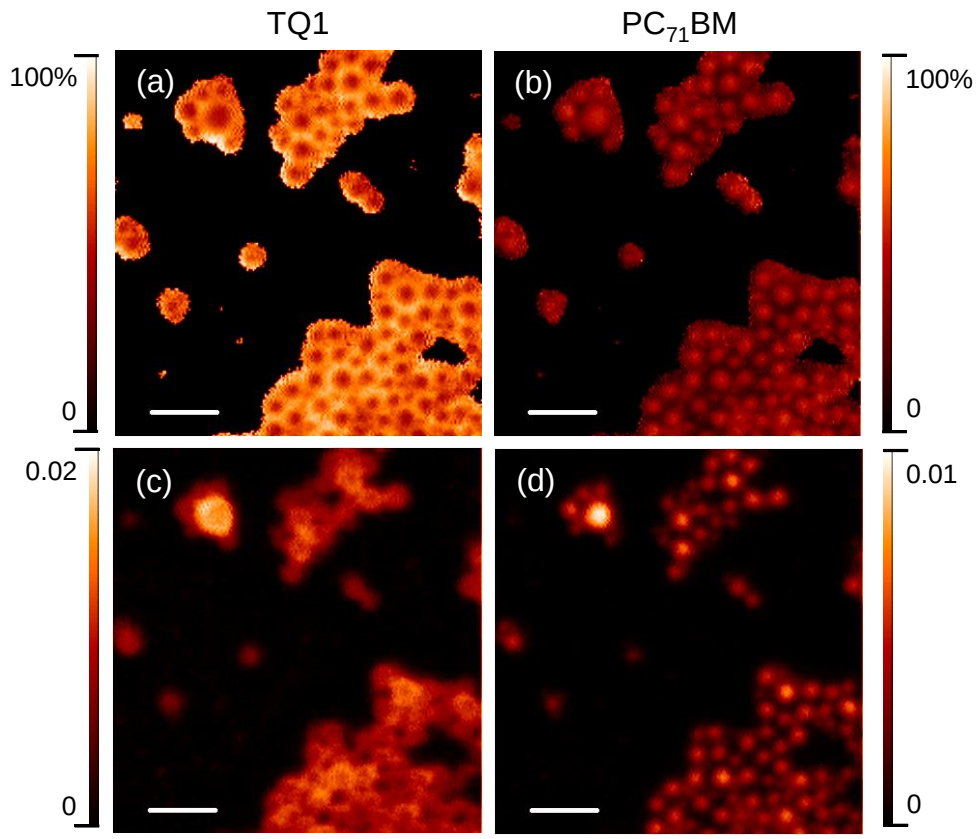

Fig. S10. STXM fractional composition maps showing the concentration of (a) TQ1 and (b) $PC_{71}BM$ with corresponding STXM mass plots (c and d) for 1:1 TQ1 : $PC_{71}BM$ nanoparticles. All scale bars are 500 nm. The colour contrast is scaled such that light colours correspond to higher component concentrations. For the mass plots (c, d) the colour scale bars indicate concentration of component in $mg.cm^{-2}$.

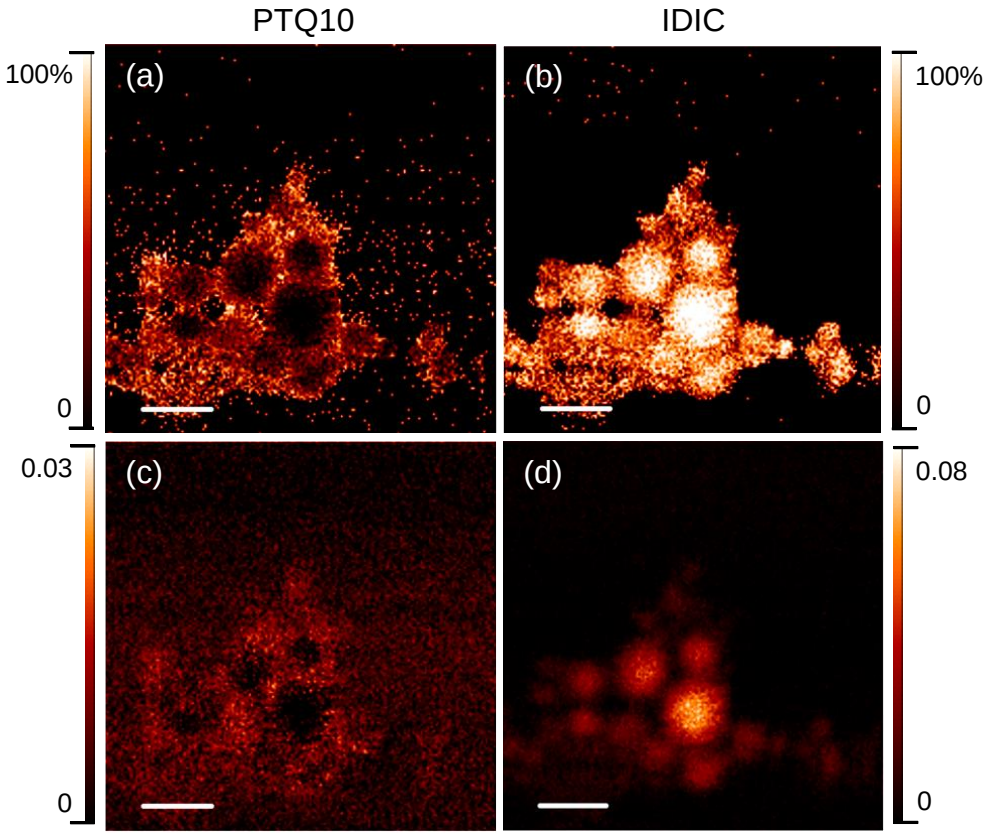

Fig. S11. STXM fractional composition maps showing the concentration of (a) PTQ10 and (b) IDIC with corresponding STXM mass plots (c and d) for 1:1 PTQ10 : IDIC nanoparticles. All scale bars are 500 nm. The colour contrast is scaled such that light colours correspond to higher component concentrations. For the mass plots (c, d) the colour scale bars indicate concentration of component in $mg.cm^{-2}$.

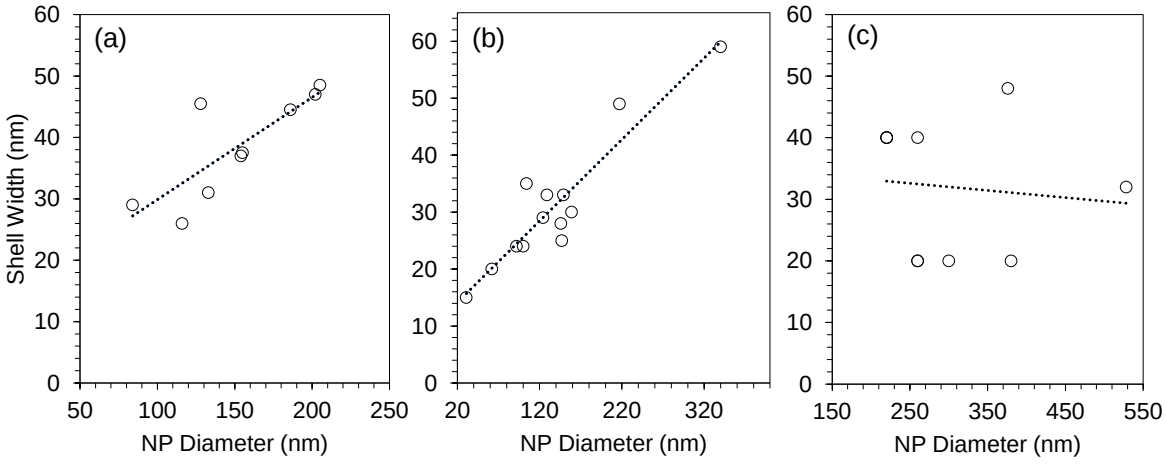

Fig. S12. Relationship between nanoparticle shell thickness and particle diameter for (a) PTzBI-Si:N2200 nanoparticles (n=9), (b) TQ1:$PC_{71}BM$ nanoparticles (n=13), and (c) PTQ10:IDIC nanoparticles (n=10).

Table S1. Comparison of STXM to STEM EDX as nanoscale mapping techniques with chemical sensitivity.

	STXM	**STEM EDX**
Technique	Synchrotron	TEM
Scanning Mode	Raster (the sample with respect to the X-ray beam)	Raster (the e^- beam with respect to the sample)
Probe particle	X-ray	Electron
Mode	Transmission	Transmission
Dimension (1D, 2D, 3D)	1D, 2D	1D, 2D
Spatial resolution	30 nm[(1)]	< 1 nm[(2,3,4)]
Spatial resolution limiting parameter	Probe size	Scattering broadening
Energy resolution	0.1 eV[1]	0.1 keV
Spectrometer range	Beamline dependent, 250-780 eV for ALS 5.3.2.2 STXM beamline	0 - 40 keV
Chemical sensitivity	Based on unique NEXAFS spectra at the C K-edge	Spatial elemental mapping
Signal interpretation	X-ray absorption cross-section	Ionisation scattering cross-section, Brown-Powell w. absorption corr.
Sample environment	Partial vacuum, 0.33 atm Helium[(5)]	Vacuum (10^{-6} mbar)
Beam induced effects	Ionisation, radiolysis	Atomic displacements, ionisation, radiolysis, charging

A STEM image post-EDX mapping is provided in Figure S12. This image shows the carbon deposition build-up only at the edge of the mapped area, which typically occurs in this region because the raster scan procedure includes delay functions in the beginning of each row and at the end of the image scan, to avoid drift and hysteresis. The scanning conditions were setup to prevent carbon deposition in the map area.

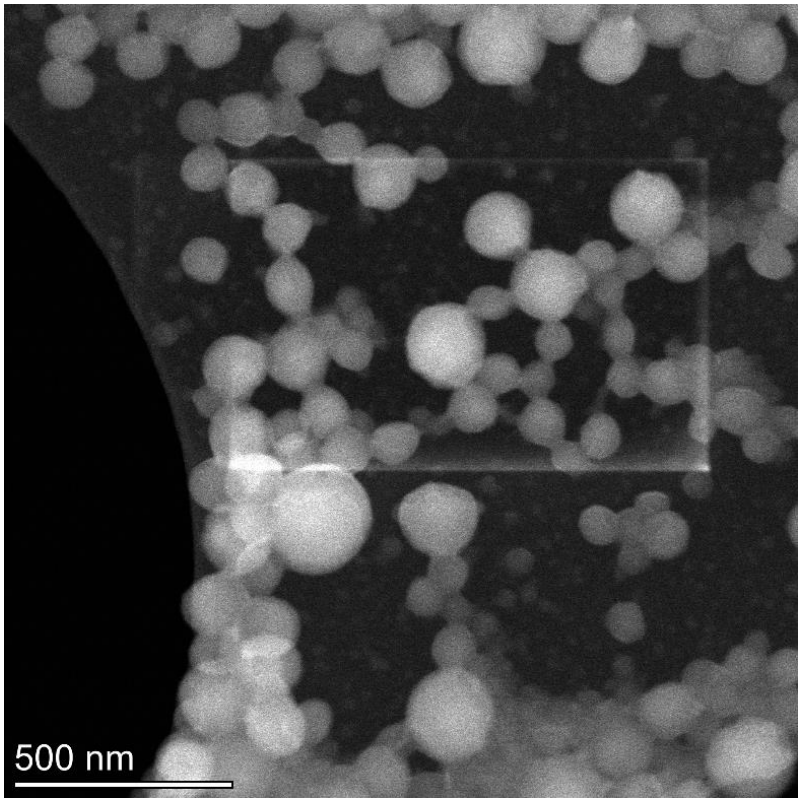

Fig. S13. STEM image showing the post-EDX scan structure of a PTzBI-Si:N2200 nanoparticle sample. C deposition is detected at the borders of the map and no observable contribution is seen within where the mapping and quantification were carried out.

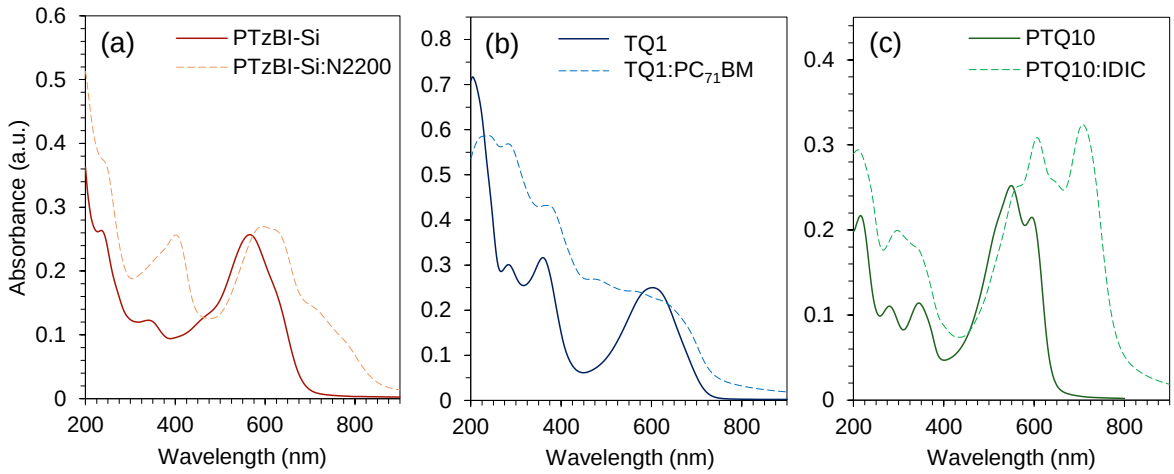

Fig. S14. UV-Visible absorbance spectra of (a) PTzBI-Si and PTzBI-Si:N2200 nanoparticles, (b) TQ1 and TQ1:$PC_{71}BM$ nanoparticles, and (c) PTQ10 and PTQ10:IDIC nanoparticles.

References

(1) Collins, B. A.; Ade, H. Quantitative Compositional Analysis of Organic Thin Films Using Transmission NEXAFS Spectroscopy in an X-Ray Microscope. *J. Electron Spectros. Relat. Phenomena* 2012, 185, 119–128.

(2) Watanabe, M.; Ackland, D. W.; Burrows, A.; Kiely, C. J.; Williams, D. B.; Krivanek, O. L.; Dellby, N.; Murfitt, M. F.: Szilagyi, Z. Improvements in the X-ray analytical

capabilities of a scanning transmission electron microscope by spherical-aberration correction, *Microsc. Microanal*. 2006, 12, 515–526.

(3) Schlossmacher, P.; Klenov, D. O.; Freitag, B.; von Harrach, H. S. Enhanced Detection Sensitivity with a New Windowless XEDS System for AEM Based on Silicon Drift Detector Technology, *Micros. Today*, 2010, 18, 14–20.

(4) Ringnalda, J.; Genc, A.; Kovarik, L. The Effect of Probe Correctors on the Analytical Results of Non-ideal Samples, *Microsc. Microanal*. 2014, 20, 566–567.

(5) Kilcoyne, A. L. D.; Tyliszczak, T.; Steele, W. F.; Fakra, S.; Hitchcock, P.; Franck, K.; Anderson, E.; Harteneck, B.; Rightor, E. G.; Mitchell, G. E.; et al. Interferometer-Controlled Scanning Transmission X-Ray Microscopes at the Advanced Light Source. *J. Synchrotron Radiat.* 2003, 10, 125–136.